This is a repository copy of *Theory and design of quantum cascade lasers in (111) n-type Si/SiGe*.

White Rose Research Online URL for this paper:
http://eprints.whiterose.ac.uk/9024/

Article:

Valavanis, A., Lever, L., Evans, C. A. et al. (2 more authors) (2008) Theory and design of quantum cascade lasers in (111) n-type Si/SiGe. Physical Review B, 78 (3). Art. No. 035420. ISSN 1098-0121

https://doi.org/10.1103/PhysRevB.78.035420

Reuse
See Attached

Takedown
If you consider content in White Rose Research Online to be in breach of UK law, please notify us by emailing eprints@whiterose.ac.uk including the URL of the record and the reason for the withdrawal request.

eprints@whiterose.ac.uk
https://eprints.whiterose.ac.uk/

Theory and design of quantum cascade lasers in (111) n-type Si/SiGe

A. Valavanis,* L. Lever, C. A. Evans, Z. Ikonić, and R. W. Kelsall
Institute of Microwaves and Photonics, School of Electronic and Electrical Engineering,
University of Leeds, Leeds LS2 9JT, United Kingdom

(Dated: July 24, 2009)

Although most work towards the realization of group IV quantum cascade lasers (QCLs) has focused on valence band transitions, there are many desirable properties associated with the conduction band. We show that the commonly cited shortcomings of n-type Si/SiGe heterostructures can be overcome by moving to the (111) growth direction. Specifically, a large band offset and low effective mass are achievable and subband degeneracy is preserved. We predict net gain up to lattice temperatures of 90 K in a bound-to-continuum QCL with a double-metal waveguide, and show that a Ge interdiffusion length of at least 8 Å across interfaces is tolerable.

PACS numbers: 73.43.Cd, 73.61.Cw, 78.45.+h, 78.67.Pt
Keywords: Silicon; germanium; SiGe; intersubband transitions; quantum cascade lasers; (111) orientation

I. INTRODUCTION

Quantum cascade lasers (QCLs) have been developed in a variety of III-V materials systems, although as yet there has been no successful demonstration in group IV. A Si/SiGe QCL would potentially reduce fabrication costs and offer a route to photonic system-on-a-chip applications.[1]

The most common approach towards a Si/SiGe QCL uses (001) oriented p-type structures,[1] and electroluminescence[2–4] has been demonstrated. There are however significant challenges in designing p-type QCLs. The coexistence of heavy and light holes leads to fast nonradiative scattering, and strong valence band mixing causes large variations in transition energies and matrix elements with in-plane wave vector.[5]

The high longitudinal effective mass of SiGe Δ valleys is commonly regarded as a major obstacle to n-type QCLs,[6] and recent theoretical investigations have used transitions in the Γ and L valleys instead.[7,8] We have however shown previously that a (111) oriented Si/SiGe QCL using Δ valley transition is viable.[9]

In this paper, we compare the strain tensors for (001) and (111) oriented layers. We show that (111) oriented Δ valleys offer larger *usable* band offsets and lower quantization effective mass than the (001) case and that complications due to subband degeneracy splitting are avoided. We summarize our calculations of the principal scattering mechanisms, current and gain, and present a bound-to-continuum QCL design in n-type (111) Si/SiGe. We calculate the waveguide losses and predict net gain in our design. Finally, we investigate the effects of temperature and nonabrupt interfaces.

II. STRAIN TENSORS

Lattice mismatch induces strain in thin $\mathrm{Si}_{1-x}\mathrm{Ge}_x$ layers on a relaxed $\mathrm{Si}_{1-x_s}\mathrm{Ge}_{x_s}$ substrate, where $x \neq x_s$. Layers below their critical thickness deform elastically to match the in-plane lattice constant of the substrate and strain balancing of a multilayer structure is required to achieve mechanical stability. This is achieved by selecting a substrate alloy which minimizes elastic potential energy with respect to in-plane strain.[10] It is convenient to convert between both the *interface* coordinate system $R = (x, y, z)$, where the z axis is normal to the layer interfaces, and the *crystallographic* coordinate system $R' = (x', y', z')$. For the (001) case, $R' = R$, whereas for (111) systems a transformation matrix $U\colon R \to R'$ is required.[11]

The in-plane strain in R is defined as

$$\varepsilon_{\|} = \frac{a_s - a}{a}, \tag{1}$$

where a is the lattice constant of the unstrained layer and a_s is that of the substrate. A good approximation for lattice constant (in nm) is[12]

$$a(x) = 0.5431 + 0.01992x + 0.0002733x^2. \tag{2}$$

Assuming isotropy over the xy plane, the strain tensors in R' for (001) and (111) oriented layers are[13]

$$\varepsilon'^{(001)} = \varepsilon_{\|} \begin{pmatrix} 1 & 0 & 0 \\ 0 & 1 & 0 \\ 0 & 0 & -\frac{2c'_{12}}{c'_{11}} \end{pmatrix}, \tag{3}$$

$$\varepsilon'^{(111)} = \frac{\varepsilon_{\|}}{c'_{\beta}} \begin{pmatrix} 4c'_{44} & c'_{\alpha} & c'_{\alpha} \\ c'_{\alpha} & 4c'_{44} & c'_{\alpha} \\ c'_{\alpha} & c'_{\alpha} & 4c'_{44} \end{pmatrix}, \tag{4}$$

where c'_{ij} are the elastic constants, $c'_{\alpha} = -(c'_{11} + 2c'_{12})$ and $c'_{\beta} = c'_{11} + 2c'_{12} + 4c'_{44}$.

The minimum average strain energy corresponds to a substrate lattice constant,[10]

$$a_s = \frac{\sum_k A_k l_k / a_k}{\sum_k A_k l_k / a_k^2}, \tag{5}$$

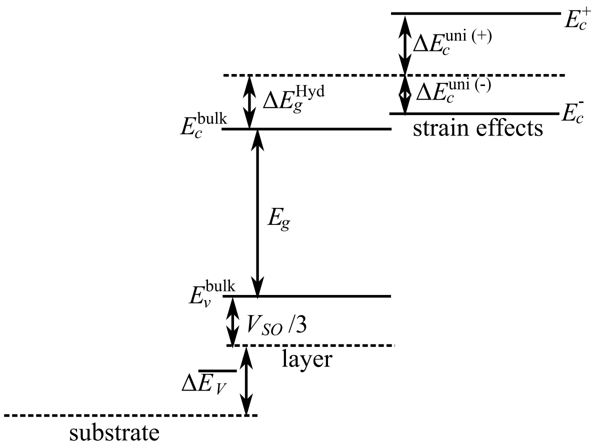

FIG. 1: Energy band schematic (not to scale) for a strained alloy layer on a rigid substrate. To find the potentials of the Δ valley minima in the strained layer, the difference in valence band energy and bandgap are calculated before adding the hydrostatic and uniaxial strain effects.

where l is the layer thickness, k is the layer index and the elastic constants are grouped into a single term A. For the (001) and (111) orientations, the elastic constants are

$$A_k^{(001)} = 2\left(c'_{11} + c'_{12} - 2\frac{c'^2_{12}}{c'_{11}}\right), \tag{6}$$

$$A_k^{(111)} = \frac{12c'_{44}(4c'_{11}c'_{44} + 8c'_{12}c'_{44} + c'^2_{\alpha})}{c'^2_{\beta}}. \tag{7}$$

III. BAND STRUCTURE

As QCLs are intersubband devices, the indirect $\text{Si}_{1-x}\text{Ge}_x$ bandgap is not an obstacle. The effective mass model for SiGe-based systems however, must account for transitions occurring away from the Γ symmetry point. The band structure is described as follows.

A. Unstrained Δ valley potential

The unstrained conduction band minima in $\text{Si}_{1-x}\text{Ge}_x$ with $x < 85\%$ are located in six degenerate valleys in k space. Each valley lies close to an X symmetry point, and has a spheroidal equipotential surface with its major axis along the associated Δ direction.[14]

The relaxed Δ valley potential relative to the substrate is determined from the model solid approximation.[15] The difference in average valence band maximum (in eV) is

$$\Delta\overline{V_{\text{VB}}} = (0.74 - 0.06x_s)(x - x_s),^{16} \tag{8}$$

and the highest valence band maximum is one third of the spin-orbit splitting above this, such that

$$\Delta V_{\text{VB}} = \Delta\overline{V_{\text{VB}}} + \frac{\Delta V_{\text{SO}}}{3}, \tag{9}$$

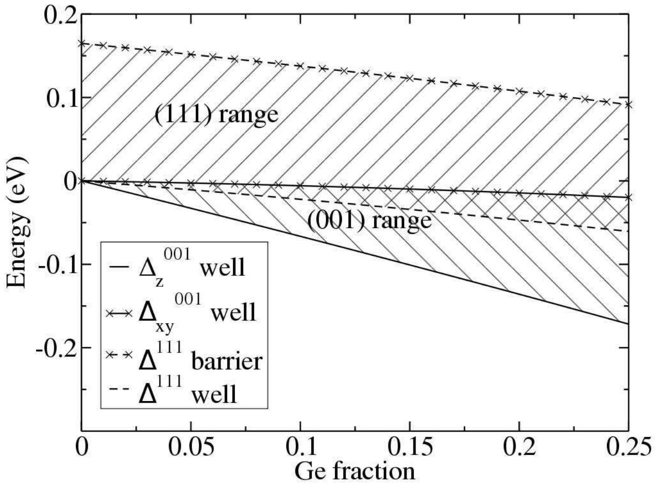

FIG. 2: Usable range of Δ-valley offsets for (111) and (001) oriented Si wells with $\text{Si}_{0.5}\text{Ge}_{0.5}$ barriers as a function of Ge fraction in the substrate. For the (111) orientation the entire quantum well may be used whereas in (001) the Δ_{xy} well potential defines the upper limit.

where ΔV_{SO} is the difference in spin orbit splitting between the two materials.[15]

The unstrained Δ valley conduction band offset is therefore

$$\Delta V_{\text{CB}} = \Delta\overline{V_{\text{VB}}} + \frac{\Delta V_{\text{SO}}}{3} + \Delta E_g, \tag{10}$$

where ΔE_g is the difference in indirect $\Gamma \rightarrow \Delta$ bandgap. To a good approximation, this is given (in eV) by[17]

$$E_g = 1.155 - 0.43x + 0.0206x^2. \tag{11}$$

B. Strained layers

In general, two strain dependent terms are added to Eqn. 10. Firstly, hydrostatic strain, *i.e.* the overall volume change, shifts the potential by an amount $\Delta V_{\text{hyd}} = a_c \operatorname{tr}(\varepsilon')$, where a_c is the hydrostatic conduction band deformation potential. For (001) heterostructures, the hydrostatic shift is

$$\Delta V_{\text{hyd}}^{(001)} = 2\left(1 - \frac{c'_{12}}{c'_{11}}\right) a_c \varepsilon_{\parallel}, \tag{12}$$

whereas for (111) heterostructures, it is

$$\Delta V_{\text{hyd}}^{(111)} = \frac{12c'_{44}}{c'_{\beta}} a_c \varepsilon_{\parallel}. \tag{13}$$

Secondly, uniaxial strain, *i.e.* the distortion from the cubic lattice form, splits the in-plane Δ_{xy} and the perpendicular Δ_z valley potentials by an amount

$$\Delta V_{\text{uni}} = \left(\frac{1}{6} \pm \frac{1}{2}\right) \Xi_{\text{u}}(\varepsilon'_{33} - \varepsilon'_{11}), \tag{14}$$

TABLE I: Quantization and average two-dimensional density-of-states effective masses, and degeneracy n of Δ valleys in (001) and (111) SiGe alloys with Ge fraction under 85%, using expressions derived from Ref. 18. Masses are expressed relative to the rest mass of a free electron.

Valley	m_q	m_d	n
$\Delta_{xy}^{(001)}$	m_t=0.19	$\sqrt{m_l m_t}$=0.42	4
$\Delta_{z}^{(001)}$	m_l=0.916	$m_t = 0.19$	2
$\Delta^{(111)}$	$\frac{3m_l m_t}{2m_l+m_t}$=0.26	$\sqrt{m_t\frac{2m_l+m_t}{3}}$=0.36	6

where Ξ_u is the uniaxial deformation potential. The upper sign represents the Δ_z valleys and the lower sign represents Δ_{xy}. This effect is absent in (111) heterostructures as strain is identical along each of the principal crystallographic axes.

The calculation is summarized in Fig. 1. The conduction band edge is generally shifted by hydrostatic strain, and in the (001) orientation, uniaxial strain splits the Δ valley degeneracy. Although intervalley optical transitions are forbidden by the wave vector shift, degeneracy splitting complicates (001) QCL design by introducing nonradiative $\Delta_z \rightarrow \Delta_{xy}$ transitions. It is therefore desirable to restrict optical transitions to energies below the Δ_{xy} valley minima.

For a strain balanced QCL with barriers narrower than wells, $x_s < 25\%$. Fig. 2 shows that the *usable* energy range in the (001) orientation decreases almost linearly with x_s from a maximum of 150 meV at x_s=25%. The (111) orientation is therefore desirable for QCL designs as the entire Δ offset of 150 meV may be used regardless of the substrate composition.

C. Effective mass

The spheroidal Δ valley approximation remains valid in strained SiGe, as the effective mass only varies slightly.[16] However, two separate effective masses are required: the longitudinal effective mass m_l=0.916 for wave vectors along the major axis of a valley and the transverse effective mass m_t=0.19 for wave vectors along the minor axes. The conduction band energy near a valley minimum is

$$E_{\mathrm{CB}} = \frac{\hbar^2}{2}\left(\frac{k_x^2}{m_x} + \frac{k_y^2}{m_y} + \frac{k_z^2}{m_z}\right), \qquad (15)$$

where $m_{x,y,z}$ are constant effective masses for momentum in a given direction in R, and $\boldsymbol{k} = k_x\hat{\boldsymbol{x}} + k_y\hat{\boldsymbol{y}} + k_z\hat{\boldsymbol{z}}$ is the wave vector relative to the subband minimum.

In QCLs, the quantization effective mass m_q describes the variation of conduction band potential in the growth direction, *i.e.* $m_q = m_z$. The density-of-states mass m_d accounts for in-plane motion and is anisotropic with respect to the in-plane wave vector. An isotropic approximation, $m_d = \sqrt{m_x m_y}$ is commonly used however.[19,20] The effective mass values are summarized in Tbl. I.

In the (001) orientation, the major axes of all four Δ_{xy} valleys lie in-plane, so $m_q = m_t$ and $m_d = \sqrt{m_t m_l}$. Conversely, the major axis of each Δ_z valley points in the growth direction, so $m_q = m_l$, while m_d is isotropic and equal to m_t.

It is slightly inaccurate to treat the Δ_z subbands as being twofold degenerate in a simple effective mass approximation (EMA) as intervalley mixing splits the degeneracy in quantum confined systems.[21] We have accounted for this in symmetric systems in a modified EMA and shown that the effect may be large in narrow quantum wells.[22] However, asymmetric structures require a computationally expensive atomistic calculation.[23,24] As the splitting is at most a few meV in weakly confined states, the effect was neglected in the QCL simulations presented in this work.

In (111) heterostructures, the situation is much simpler. All six Δ valleys have $m_q = 0.26$ and identical confining potentials. Intervalley mixing is absent as each valley lies at a different value of k_{xy}. The subbands are therefore sixfold degenerate within the EMA.

In summary, the conduction band for (001) heterostructures is complicated by effective mass anisotropy. The Δ_z subbands may conceivably be used for QCL design, but the large m_q value severely limits the oscillator strength and hence the gain.[14] The Δ_{xy} subbands have lower m_q, but states are weakly confined by the small band offsets and have low populations due to their high energy.

The (111) orientation however, offers both low effective mass and high band offset and shows more promise for QCL designs. The low mass allows wider wells to be used than for Δ_z transitions in (001) systems. QCL designs in the (111) orientation are therefore more tolerant to deviations in layer thicknesses caused by growth errors.

IV. CARRIER TRANSPORT MODEL

Having established the differences in band structure and effective mass between (001) and (111) oriented heterostructures, carrier transport may now be modeled in QCL structures. Detailed quantum theoretical approaches have been used to simulate intersubband optical emissions in quantum wells[25] and carrier transport in limited numbers of subbands in QCLs.[26] They are, however, too computationally demanding for use as design tools for large multi-level QCLs.

Reasonably good agreement has been achieved between experimental results and Boltzmann or rate equation based models of bound-to-continuum THz QCLs in III–V systems.[27,28] In the present work, we have therefore determined subband populations using a computationally efficient rate equation approach.[28] This has been described in more detail previously,[29] although a brief summary follows.

Several intravalley scattering mechanisms are important in Si/SiGe systems. Interface roughness scattering was calculated using the correlated Gaussian roughness model,[30] modified for arbitrary interface geometries[29] and alloy disorder scattering was calculated using a point perturbation model.[31,32] Ionized impurity scattering was determined using a Coulombic interaction model as described by Unuma[33] with Thomas-Fermi screening,[14] while electron-electron scattering was treated as a screened Coulombic interaction as described by Smet.[34] The intravalley deformation potential scattering for electron-acoustic phonon interactions was also included.

Intervalley electron-phonon scattering was determined only for the Si-Si branch of the deformation potential interaction, as the Ge fraction in quantum wells is small. The f processes, which transfer electrons to the perpendicular valleys, are faster than g processes which transfer electrons to the opposite valley, due to the larger number of destination states.[35] Of the f processes, the f-LA (phonon energy $\hbar\omega_0 = 46.3\,\text{meV}^{36}$) and f-TO ($\hbar\omega_0 = 59.1\,\text{meV}^{36}$) interactions are rapid zero-order terms in the scattering model.[37] Scattering rates increase rapidly with transition energy, and saturate above the phonon energy.

The electron transfer rate from initial subband i to final subband f is the product of the average intersubband scattering rate $\overline{W}_{if}$ (due to all scattering processes) and the initial subband population N_i. Although a simple estimate of current density is proportional to the total electron transfer rate,[38] an improved model takes account of the spatial separation of electrons. The current density is therefore

$$J = \frac{q_e}{L_p} \sum_i N_i \sum_f \overline{W}_{if} \left(\langle z \rangle_f - \langle z \rangle_i \right), \tag{16}$$

where q_e is the electronic charge, L_p is the length of a structural period and $\langle z \rangle$ is the expectation value of the position operator.

The active region gain or absorption for each transition was calculated as[28]

$$G_{if}(\omega) = \frac{e^2 \omega \pi}{c n_0 \epsilon_0 L_p} N_i |z_{if}|^2 \operatorname{sgn}(E_{if}) L(\omega, E_{if}), \tag{17}$$

where n_0 is the refractive index of Si, ϵ_0 is the permittivity of free space, and c is the speed of light *in vacuo*. E_{if} is the energy difference between the subband minima, sgn$(\cdot)$ is the signum function, z_{if} is the dipole matrix element, and $L(\omega, E_{if})$ is the lineshape for the transition. The gain spectrum is found by summing Eqn. 17 over all transitions.

Although linewidth may be obtained directly from our scattering rate calculations,[33] or from more sophisticated models,[25] several important implementation issues, such as how to treat the extremely broad absorptions into weakly bound higher energy subbands, are beyond the scope of the present work. Normalized Lorentzian lineshapes centered about E_{if} have been observed in THz III-V systems, with full-width at half-maximum around 2 meV at low temperatures.[27] We therefore calculated gain spectra using linewidths in the range 1.5–2.5 meV. At higher lattice temperatures, the increased scattering rates cause linewidth broadening,[25,39] and consequently we expect our higher linewidth results to be more realistic at higher temperatures.

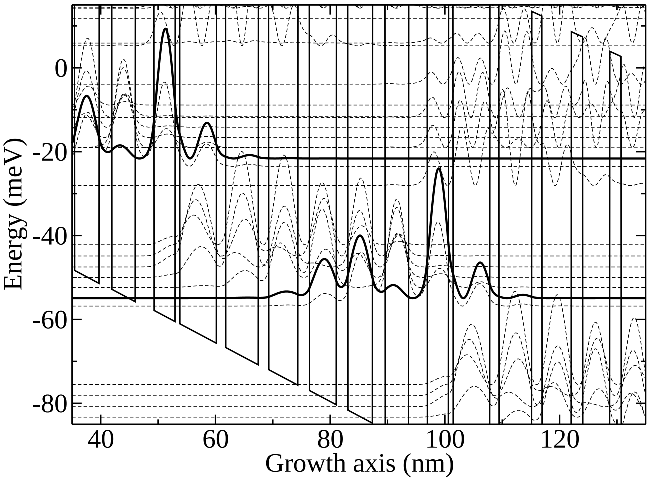

FIG. 3: A seven-well bound-to-continuum QCL at a bias of 7 kVcm^{-1} with layer widths of **3.2**/3.7/**0.8**/6.4/**1.6**/5.7/**1.8**/5.1/**2.0**/4.7/**2.0**/4.3/**2.2**/4.1, where boldface denotes 40% Ge barriers and lightface denotes pure Si wells. Dopants are spread evenly through the structure with a concentration of 5×10^{16} cm^{-3}. The conduction band potential (solid line) is shown, with spatially dependent probability densities superimposed at each subband minimum. The upper laser subband is shown in bold, while other subbands are shown as dashed lines.

V. QCL PERFORMANCE

We have described the advantages of the (111) orientation for Si/SiGe QCLs in general terms and have previously predicted net gain in a novel phonon depopulation QCL.[9] In this section, we present a bound-to-continuum active region design with a double-metal waveguide and demonstrate that net gain is achievable up to 90 K. We also show that reasonable limitations in growth quality due to interdiffusion do not present a significant obstacle.

A. Active region design

The band structure in a seven-well bound-to-continuum QCL was calculated using a single band EMA and is shown in Fig. 3 for a 7 kVcm^{-1} applied electric field. Non-radiative depopulation of the upper laser subband was reduced by limiting the higher energy scattering processes. Pure Si wells were used to minimize alloy disorder scattering, and a relatively low Ge composition

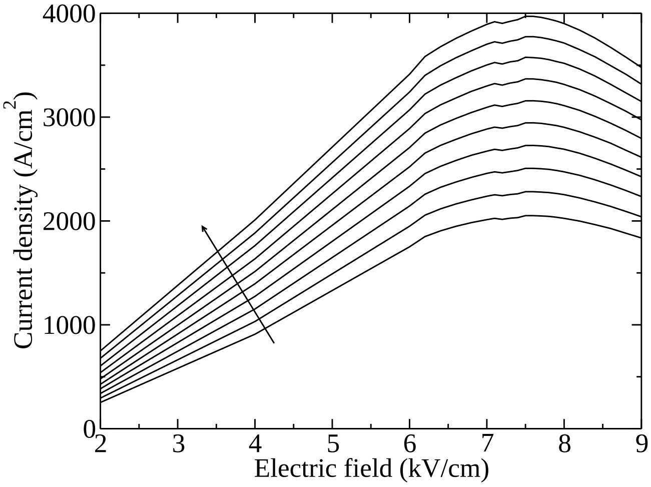

FIG. 4: Current density as a function of applied electric field for the QCL design in Fig. 3. Results are shown for linearly increasing lattice temperatures, in the direction of the arrow, between 4 and 100 K.

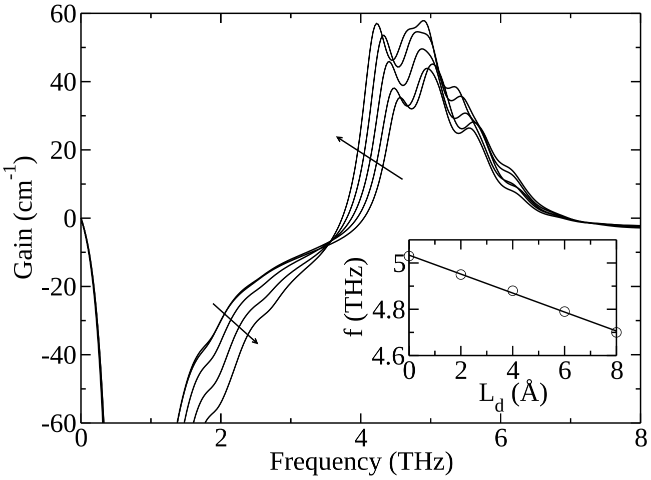

FIG. 5: Active region gain at 7 kVcm^{-1}, and 4 K lattice temperature as a function of THz frequency for the design in Fig. 3. Arrows indicate linearly increasing diffusion lengths from 0 to 8 Å. The resulting frequency shift of the largest gain peak is shown inset.

of 40% was selected for the barriers to reduce interface roughness scattering. The optical transition energy was chosen to be significantly smaller than 46.3 meV to reduce f-LA and f-TO phonon emission rates.

As modulation doping of donors in Si/SiGe heterostructures may be difficult,[40] dopants were assumed to be spread evenly throughout the structure. It was also assumed that all donors were ionized at low temperatures. A donor concentration of 5×10^{16} cm^{-3} (sheet doping density of 2.4×10^{11} cm^{-2}) caused negligible internal electric fields, while still allowing rapid depopulation of upper miniband states by Coulombic scattering.

Figure 5 shows gain at frequencies around 5 THz, due to transitions from the upper laser subband to upper miniband states, for 4 K lattice temperature and 7 kVcm^{-1} applied electric field. Figure 4 shows that a current density of 2 kAcm^{-1} corresponds to these conditions, and doubles as lattice temperature increases to 100 K. An energy balance approach[28] was used to find electron temperatures. Assuming an identical temperature in each subband, we found that electron temperatures increased from 110 to 150 K as lattice temperatures increased from 4 to 100 K.

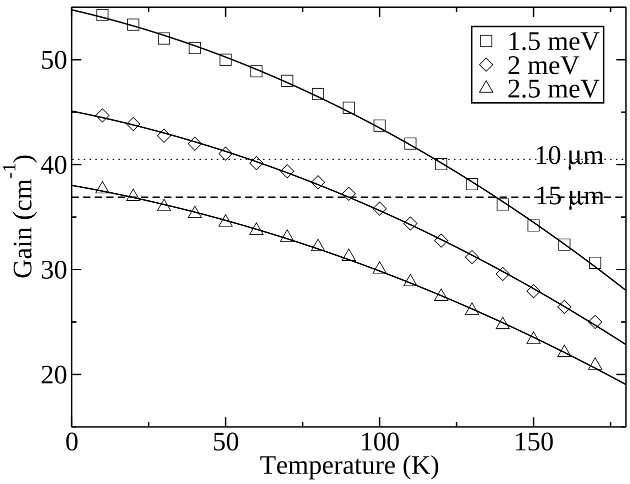

FIG. 6: Peak gain near 5 THz as a function of lattice temperature for the QCL design in Fig. 3. Results are given for linewidths of 1.5, 2.0 and 2.5 meV. The threshold gains for 10 and 15 μm active region thicknesses are shown as dotted and dashed lines respectively.

Figure 6 shows the peak gain near 5 THz as a function of lattice temperature for 1.5, 2.0 and 2.5 meV transition linewidths. As discussed in section IV, linewidth increases with temperature, and we expect the low-temperature gain to be enhanced and the high-temperature gain to be limited accordingly.

To provide a fair comparison with Δ_z subbands in the (001) orientation, an equivalent (001) design was developed. Firstly, the Δ_z conduction band offset was matched to that of the (111) design by setting the barrier Ge fraction to 26%. Noting that the subband energies are much smaller than the barrier energy, an infinite quantum well approximation was used to transform the layer widths and preserve subband separation,

$$l_k^{(001)} = l_k^{(111)} \sqrt{\frac{m_q^{(111)}}{m_q^{(001)}}} = 0.533 l_k^{(111)}. \tag{18}$$

This scaling also preserves the barrier transparency, *i.e.* the coupling between adjacent wells. Finally, the applied electric field was increased to 13.1 kVcm^{-1} to account for the reduced period length.

The Δ_z subbands in the (001) system were at sufficiently low energy compared with the Δ_{xy} valleys, for f-phonon interactions to be negligible. With the larger electric field, and with only slow g-phonon interactions available to cool the electron distribution, the steady-state electron temperature was greatly increased to 290 K for a lattice temperature of 4 K. Consequently, thermal backscattering led to a much lower peak gain coefficient of $0.2\,\mathrm{cm}^{-1}$ at 6 THz, corresponding to a current density of $1.1\,\mathrm{kAcm}^{-1}$. Growth of such a structure is also expected to be challenging, as the minimum layer thickness was reduced to 4 Å.

B. Waveguide design

A suitable waveguide was designed using a one-dimensional simulation. The propagation constant was obtained using a transfer matrix method[41] and the complex permittivities were found using the bulk Drude model using Si/SiGe material parameters from Ref. 42. The active region was modelled as bulk $\mathrm{Si}_{0.9}\mathrm{Ge}_{0.1}$ (to match the virtual substrate), with a doping concentration of $5 \times 10^{16}\,\mathrm{cm}^{-3}$.

Surface-plasmon configurations[27] were found to be unsuitable, due to the low confinement factor Γ and large waveguide losses α_w. We therefore chose a metal-metal configuration, which has proved successful in GaAs-based THz QCLs.[43] The active region was enclosed between a pair of highly doped ($n = 10^{19}\,\mathrm{cm}^{-3}$), 20 nm thick Si layers, followed by the metallic layers. The optical properties of the metallic layers are given in Ref. 44.

An initial design, using gold metallic layers and a $10\,\mu$m thick active region gave α_w=$50.7\,\mathrm{cm}^{-1}$ and Γ=0.99. Assuming mirror losses of $\alpha_\mathrm{m} = 1\,\mathrm{cm}^{-1}$,[45] the threshold gain was determined as $g_\mathrm{Th} = (\alpha_\mathrm{w} + \alpha_\mathrm{m})/\Gamma = 51.7\,\mathrm{cm}^{-1}$, which was too high to achieve lasing.

The highest temperature operation of a GaAs-based THz QCL was achieved recently by using copper instead of gold layers.[46] Incorporating this into our waveguide reduces the threshold gain to $40.5\,\mathrm{cm}^{-1}$. As shown in Fig. 6, this permits lasing up to T=58 K for a 2 meV linewidth. By increasing the active region thickness to $15\,\mu$m, the threshold gain was reduced further to $36.9\,\mathrm{cm}^{-1}$, which permits lasing up to T=90 K.

C. Growth variations

We restricted our (111) design to layer thicknesses above 8 Å as Si/SiGe epitaxy is not as well established as in III-V systems. The thinnest barrier would ideally be thinner than this to increase the dipole matrix element between the bound subband and the upper miniband states. The requirement for thin barriers is less important in (111) heterostructures than in (001) however, as the quantization effective mass is smaller and the matrix element is larger.

Ge surface segregation has been observed in (001) heterostructures,[40] and presumably this will also be the case in (111) systems. The geometry of the thinnest layers in a QCL is expected to change considerably as a result. We have previously shown however, that a limited amount of interdiffusion is tolerable, although changes in transition energies are expected.[29]

Figure 5 shows that gain increases slightly as a function of interdiffusion length, L_d up to 8 Å for our QCL design. This is due to the thinnest barrier being degraded, increasing the dipole matrix element for optical transitions. The inset in the figure shows that the center of the largest gain peak correspondingly shifts from around 5 to 4.7 THz, as the upper laser subband energy decreases.[29]

VI. CONCLUSION

We have shown that intersubband lasing in the Δ valleys of Si/SiGe heterostructures becomes viable in the (111) orientation. Although the Δ_z conduction band offset in the (001) orientation is large, the *usable* energy range was shown to be superior in the (111) orientation due to the sixfold valley degeneracy. The quantization effective mass was also shown to be much smaller in (111) heterostructures, and complications due to intervalley mixing and uniaxial strain splitting are avoided.

We have presented a bound-to-continuum design for a (111) Si/SiGe QCL and investigated several options for waveguides. A surface-plasmon waveguide was shown to be inadequate, while good results were achieved for a double-metal configuration using copper metallic layers. We have shown using a self-consistent rate-equation/energy balance calculation that net gain at 5 THz is possible up to a lattice temperature of 90 K, with a low-temperature current density of $2\,\mathrm{kAcm}^{-1}$ for a $15\,\mu$m thick active region.

The (111) design was found to be vastly superior to a (001) oriented equivalent, due to the phonon-mediated electron cooling and the reduced effective mass. It was also shown to be tolerant to, and indeed improve slightly, with Ge interdiffusion lengths up to 8 Å.

Acknowledgments

This work is supported by EPSRC Doctoral Training Allowance funding and DTI-MNT contract 491: "Fast THz Cameras".

---

[*] Electronic address: `a.valavanis05@leeds.ac.uk`

[1] R. W. Kelsall, Z. Ikonić, P. Harrison, S. A. Lynch,

R. Bates, D. J. Paul, D. J. Norris, S. L. Liew, A. G. Cullis, D. J. Robbins, et al., in *Towards the First Silicon Laser*, edited by L. Pavesi, S. Gaponenko, and L. D. Negro (Kluwer Academic Publishers, Dordrecht, 2003), vol. 93 of *NATO Science Series II: Mathematics, Physics and Chemistry*, pp. 367–382.

[2] G. Dehlinger, L. Diehl, U. Gennser, H. Sigg, J. Faist, K. Ensslin, D. Grutzmacher, and E. Muller, Science **290**, 2277 (2000).

[3] D. Paul, S. Lynch, R. Bates, Z. Ikonić, R. Kelsall, P. Harrison, D. Norris, S. Liew, A. Cullis, D. Arnone, et al., Physica E **16**, 147 (2003).

[4] S. A. Lynch, R. Bates, D. J. Paul, D. J. Norris, A. G. Cullis, Z. Ikonic, R. W. Kelsall, P. Harrison, D. D. Arnone, and C. R. Pidgeon, Appl. Phys. Lett. **81**, 1543 (2002).

[5] Z. Ikonić, P. Harrison, and R. W. Kelsall, Phys. Rev. B **64**, 245311 (2001).

[6] D. J. Paul, Semicond. Sci. Tech. **19**, R75 (2004).

[7] G. Han and J. Yu, Semicond. Sci. Tech. **22**, 769 (2007).

[8] K. Driscoll and R. Paiella, Appl. Phys. Lett. **89**, 191110 (2006).

[9] L. Lever, A. Valavanis, Z. Ikonić, and R. W. Kelsall, Appl. Phys. Lett. **92**, 021124 (2008).

[10] P. Harrison, *Quantum Wells, Wires and Dots* (Wiley, Chichester, 2005), 2nd ed.

[11] J. M. Hinckley and J. Singh, Phys. Rev. B **42**, 3546 (1990).

[12] V. Bublik, S. Gorelik, A. Zaitsev, and A. Polyakov, Phys. Status Solidi **65**, K79 (1974).

[13] S. Smirnov and H. Kosina, Solid State Electron. **48**, 1325 (2004).

[14] J. H. Davies, *The Physics of Low-Dimensional Semiconductors: An Introduction* (Cambridge University Press, Cambridge, 1998).

[15] C. G. Van de Walle, Phys. Rev. B **39**, 1871 (1989).

[16] M. M. Rieger and P. Vogl, Phys. Rev. B **48**, 14276 (1993).

[17] J. Weber and M. I. Alonso, Phys. Rev. B **40**, 5683 (1989).

[18] A. Rahman, M. S. Lundstrom, and A. W. Ghosh, J. Appl. Phys. **97**, 053702 (2005).

[19] A. Schenk, J. Appl. Phys. **79**, 814 (1996).

[20] H. Mizuno, K. Taniguchi, and C. Hamaguchi, Phys. Rev. B **48**, 1512 (1993).

[21] F. J. Ohkawa and Y. Uemura, J. Phys. Soc. Jpn. **43**, 907 (1977).

[22] A. Valavanis, Z. Ikonić, and R. W. Kelsall, Phys. Rev. B **75**, 205332 (2007).

[23] T. B. Boykin, G. Klimeck, M. Friesen, S. N. Coppersmith, P. von Allmen, F. Oyafuso, and S. Lee, Phys. Rev. B **70**, 165325 (2004).

[24] M. Friesen, S. Chutia, C. Tahan, and S. N. Coppersmith, Phys. Rev. B **75**, 115318 (2007).

[25] I. Waldmüller, J. Förstner, S.-C. Lee, A. Knorr, M. Woerner, K. Reimann, R. A. Kaindl, T. Elsaesser, R. Hey, and K. H. Ploog, Phys. Rev. B **69**, 205307 (2004).

[26] S.-C. Lee and A. Wacker, Phys. Rev. B **66**, 245314 (2002).

[27] R. Köhler, A. Tredicucci, F. Beltram, H. E. Beere, E. H. Linfield, A. G. Davies, D. A. Ritchie, R. C. Iotti, and F. Rossi, Nature **417**, 156 (2002).

[28] V. D. Jovanovic, S. Hofling, D. Indjin, N. Vukmirovic, Z. Ikonic, P. Harrison, J. P. Reithmaier, and A. Forchel, J. Appl. Phys. **99**, 103106 (2006).

[29] A. Valavanis, Z. Ikonić, and R. W. Kelsall, Phys. Rev. B **77**, 075312 (2008).

[30] T. Ando, A. B. Fowler, and F. Stern, Rev. Mod. Phys. **54**, 437 (1982).

[31] D. N. Quang, N. H. Tung, D. T. Hien, and H. A. Huy, Phys. Rev. B **75**, 073305 (2007).

[32] F. Murphy-Armando and S. Fahy, Phys. Rev. Lett. **97**, 096606 (2006).

[33] T. Unuma, M. Yoshita, T. Noda, H. Sakaki, and H. Akiyama, J. Appl. Phys. **93**, 1586 (2003).

[34] J. H. Smet, C. G. Fonstad, and Q. Hu, J. Appl. Phys. **79**, 9305 (1996).

[35] C. Canali, C. Jacoboni, F. Nava, G. Ottaviani, and A. Alberigi-Quaranta, Phys. Rev. B **12**, 2265 (1975).

[36] P. Dollfus, J. Appl. Phys. **82**, 3911 (1997).

[37] F. Monsef, P. Dollfus, S. Galdin, and A. Bournel, Phys. Rev. B **65**, 212304 (2002).

[38] Z. Ikonic, P. Harrison, and R. W. Kelsall, J. Appl. Phys. **96**, 6803 (2004).

[39] H. Page, C. Becker, A. Robertson, G. Glastre, V. Ortiz, and C. Sirtori, Appl. Phys. Lett. **78**, 3529 (2001).

[40] J. Zhang, S. Turner, S. Chiam, R. Liu, E. Tok, A. Wee, A. Huan, I. Kelly, and C. Mulcahy, Surf. Sci. **600**, 2288 (2006).

[41] E. Anemogiannis, E. Glytsis, and T. Gaylord, J. Lightwave Technol. **17**, 929 (1999).

[42] V. Palankovski, Ph.D. thesis, Technischen Universität Wien (2000).

[43] B. S. Williams, S. Kumar, H. Callebaut, Q. Hu, and J. L. Reno, Appl. Phys. Lett. **83**, 2124 (2003).

[44] M. A. Ordal, R. J. Bell, J. R. W. Alexander, L. L. Long, and M. R. Querry, Appl. Opt. **24**, 4493 (1985).

[45] S. Kohen, B. S. Williams, and Q. Hu, J. Appl. Phys **97**, 053106 (2005).

[46] M. A. Belkin, J. A. Fan, S. Hormoz, F. Capasso, S. P. Khanna, M. Lachab, A. G. Davies, and E. H. Linfield, Opt. Express **16**, 3242 (2008).